Chapter 5

Comparision of co-seismic and post-seismic slip from the November 12, 1996, M_w 7.7 and the June 23, 2001, M_w 8.4 southern Peru subduction zone earthquakes

Abstract

We use InSAR and GPS observations to constrain co-seismic and post-seismic slip from the November 12, 1996, M_w 7.7 and June 23, 2001, M_w 8.4 southern Peru subduction zone earthquakes. Using InSAR data from six tracks of the ERS and JERS satellites, we find that the 1996 earthquake ruptured to a maximum depth of about 60 km. For the 2001 earthquake, we find a maximum depth of between 50-60 km, using four tracks of data from ascending and descending orbits of the ERS satellite along with GPS observations from the Arequipa station. Both earthquakes appear to rupture to the bottom of the seismogenic zone. Interferograms spanning 50 days to three years after the 1996 earthquake reveal no post-seismic deformation, while the continuous GPS station in Arequipa records that about 20% of the co-seismic moment was released in the first nine months following the 2001 earthquake. We compare the co-seismic and post-seismic slip distributions from the 1996 and 2001 earthquakes with the 1995 M_w 8.1 Antofagasta, Chile, earthquake. All three events rupture to the south, and while this seems to be true of several recent South American subduction zone earthquakes, the reason for this common directivity is unknown. Variations in the amount of afterslip following the 1995, 1996 and 2001 earthquakes is possibly related to variations in the sediment subducted in each location.

5.1 Introduction

In addition to the 1995 M_w 8.1 Antofagasta, Chile, earthquake (Chapters 3 and 4), there have been two other large subduction zone earthquakes within our study area during the past 10 years. In Figure 5.1, we show interferograms for the 12 November 1996 M_w 7.7 Nazca, Peru, and the 23 June 2001 M_w 8.4 Arequipa, Peru, earthquakes (hereafter referred to as the 1996 and 2001 earthquakes) as well as the 1995 Chile earthquake. We use InSAR and GPS data to determine magnitudes and distributions of co-seismic and post-seismic slip from the earthquakes in southern Peru. We compare these three events to better understand rupture characteristics of these large earthquakes as well as along-strike variations in the subduction zone earthquake cycle.

Although the 1995, 1996 and 2001 events are all shallow thrust earthquakes, they look slightly different in Figure 5.1. To first order, the different appearance of the interferograms for these three events is due to the location of slip on the fault interface relative to the coastline, and the size of each earthquake. Because InSAR measures primarily vertical deformation, we can interpret the gross features of the interferograms as portions of the ground that were uplifted or subsided. Detailed interpretation of the deformation pattern must account for the different radar LOS relative to the direction of slip. As shown in Figure 3.7, most of the co-seismic uplift from shallow subduction zone thrust earthquakes is located off-shore. For the 1995 earthquake, only part of the dry land was uplifted (the south-west corner of the Mejillones Peninsula), and the closed contours in the interferogram are mostly caused by the on-land subsidence. For the 1996 earthquake, the slip was closer to land (as suggested by the CMT location), so that more uplift is recorded on-shore and the closed contours of the subsidence basin are further inland. Most of the fault slip from the 2001 earthquake was off-shore, so only a portion of the subsidence basin is seen on land. Although less of the deformation pattern from the 2001 earthquake is on shore, because of the larger size of the 2001 event, we measure the maximum LOS component of deformation from this earthquake.
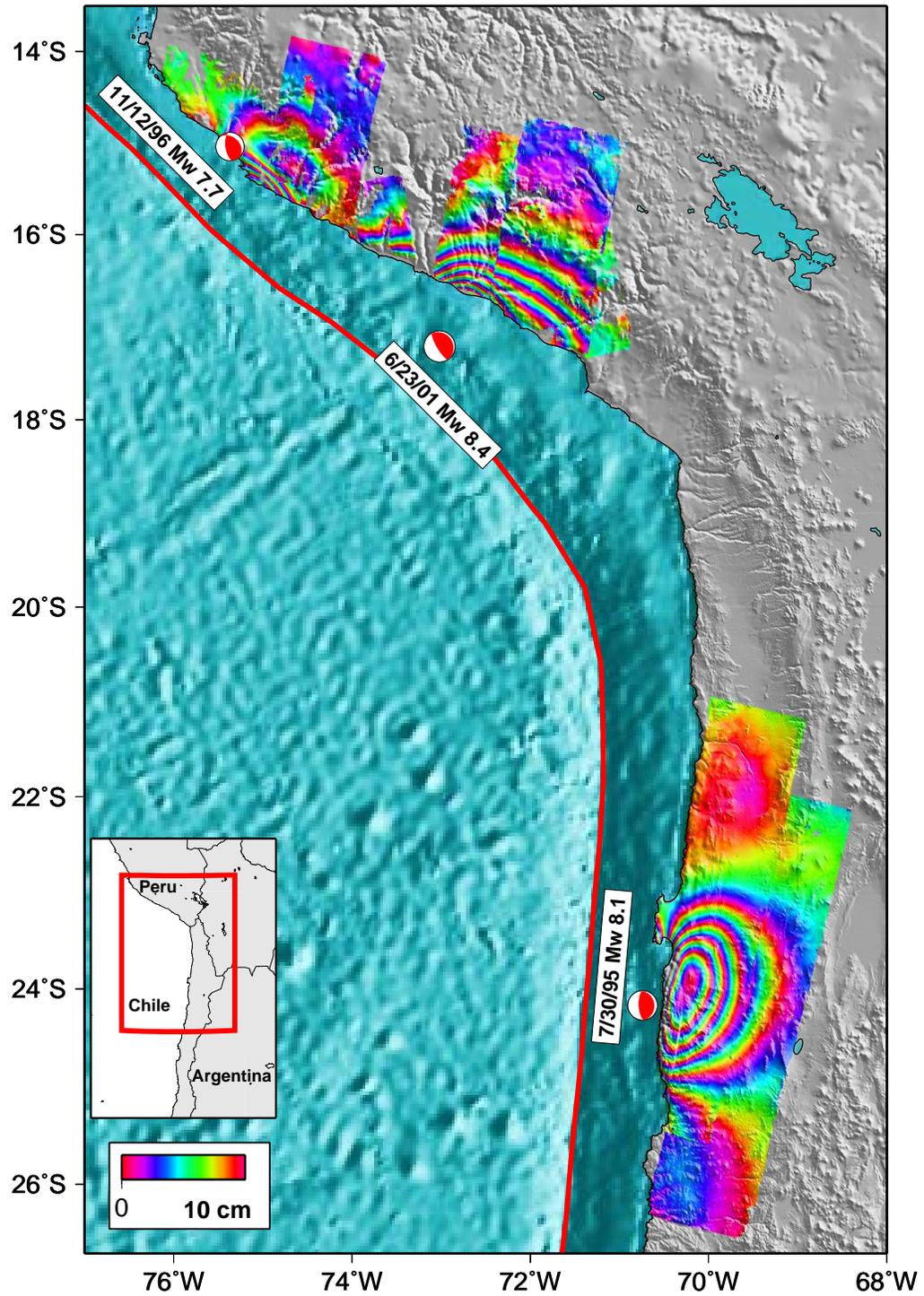
Figure 5.1: ERS interferograms of three large subduction zone earthquakes draped over shaded relief and bathymetry. The dates of the interferograms are shown in Table 4.1 (tracks 96 and 325) and Table 5.1. The Harvard CMT mechanisms are shown along with the trench location (red line) and the reference map in the lower left.

5.2 Previous work

The rupture process of the 1996 earthquake has been constrained with teleseismic data (*Swenson and Beck*, 1999; *Spence et al.*, 1999) and teleseismic data coupled with one ERS interferogram (*Salichon et al.*, 2003). For the 2001 event, teleseismic data (*Giovanni et al.*, 2002; *Bilek and Ruff*, 2002) and displacements from a single GPS station (*Ruegg et al.*, 2001; *Melbourne and Webb*, 2002) have been used. The 2001 event generated a large tsunami with wave peaks of 7 m (*Okal et al.*, 2001). There are no local reports of a tsunami from the 1996 earthquake, and the nearest tide gauge in Arica, Chile (more than 600 km away from the hypocenter) recorded a run-up of less than 0.33 m (*Swenson and Beck*, 1999).
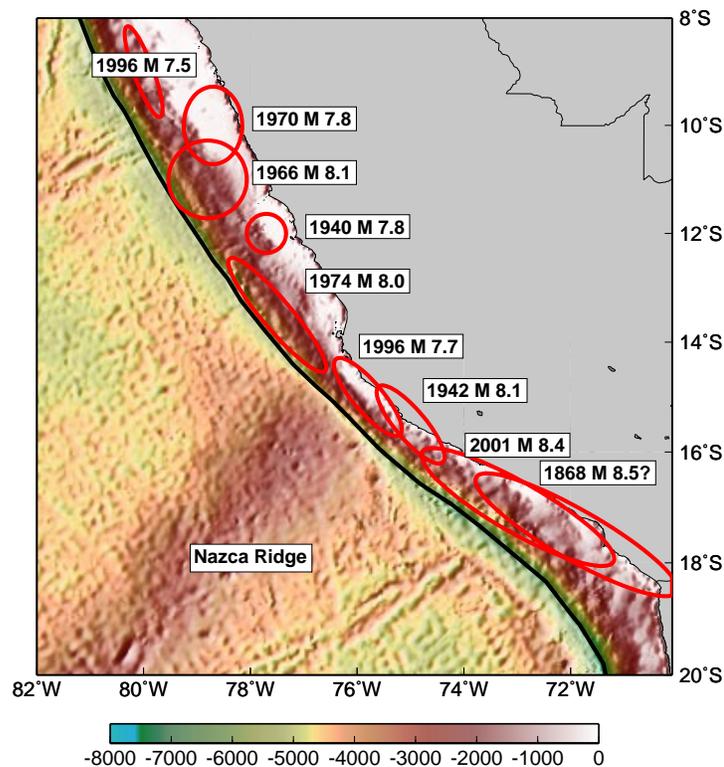
Figure 5.2: Estimated rupture zones for earthquakes in southern Peru during the past 150 years with dates and approximate moments (e.g., *Beck and Ruff*, 1989; *Swenson and Beck*, 1996; *Spence et al.*, 1999; *Giovanni et al.*, 2002).

The 1996 event rupture area partly overlaps the region that slipped in an M_w 8.1 earthquake in 1942, as well as the region where the Nazca Ridge is being subducted (Figure 5.2, *Chatelain et al.*, 1997; *Swenson and Beck*, 1996; *Spence et al.*, 1999). While oceanic ridges and seamounts are observed to have low rates of seismicity in some areas, the 1996 earthquake and others (*e.g.,* the 1985 Mexico earthquake) indicate that large earthquakes can be associated with these bathymetric features (e.g., *Spence et al.*, 1999). The coastal uplift from the 1996 earthquake occurred near a region of long-term coastal uplift, and several authors have suggested that numerous earthquakes similar to the 1996 event caused this uplift (*Swenson and Beck*, 1999; *Spence et al.*, 1999; *Salichon et al.*, 2003). The 2001 earthquake partly re-ruptured the area of the great 1868 earthquake, although the area of the 1868 event is not well constrained (*Giovanni et al.*, 2002; *Bilek and Ruff*, 2002).

Our study is complementary to the previous work, because our extensive images of surface deformation can constrain the spatial extent of slip, particularly in depth. To understand the possible coupling between co-seismic slip and afterslip, the distribution of slip as a function of depth must be well constrained. In particular, for the 1996 earthquake, there are conflicting reports of the depth of rupture, with one model favoring slip to 66 km (*Spence et al.*, 1999) and another to only 40 km (*Salichon et al.*, 2003).

5.3   Data used

For the 1996 earthquake, we have six interferograms from six different descending orbital tracks – three from ERS and three from JERS (Figure 5.3), see Table 5.1 for details. The ERS and JERS data have different sensitivities to horizontal motion (LOS angles 23° from vertical for ERS, and 44° for JERS). Thus, although we only have data from descending orbits, we recover more than one component of deformation. Furthermore, the interferograms from the different orbital tracks overlap and have slightly different viewing geometry for a given ground location. In the interferograms, we measure a maximum deformation in the LOS of about 0.35 m. All of the

interferograms include inter-seismic deformation (up to 5.5 years) and at least several months of post-seismic deformation.

There is little additional deformation data available for this earthquake. A GPS array within the rupture area was occupied in June 1996 and July 2001, so displacements include inter-seismic, post-seismic, and co-seismic deformation (from both the 1996 and 2001 earthquakes). A preliminary analysis indicates that three stations show co-seismic displacements of up to 90 cm of horizontal and vertical motion (T. Dixon and E. Norabuena, personal communication, 2001). Coastal uplift of up to 20 cm was observed, but not systematically documented (*Chatelain et al.*, 1997).

Earthquake	Track	Frame(s)	Master image	Slave image	$B_\perp$ (m)
	311	3897-3915	23 May 1992	22 Sep. 1997	125
	82	3897	27 May 1993	12 Oct. 1997	230
	39	3897-3915	9 Oct. 1997	24 Oct. 1996	100
Nazca EQ	p429	325-326	4 Mar. 1994	21 Apr. 1997	250
	p430	325-326	9 Mar. 1997	19 May 1995	200
	p431	325	10 Mar. 1997	29 Oct. 1996	900
	311	4059	22 Sep. 1997	7 Dec. 1999	80
Nazca post-seismic	39	4059	9 Oct. 1997	23 Dec. 1999	160
	39	4059	2 Jan. 1997	8 Oct. 1997	170
	225	3915-3951	9 Apr. 1996	9 Jan. 2002	40
	454	3915-3951	2 Nov. 1995	21 Dec. 2001	110
Arequipa EQ	89	6849-6867	10 Jan. 1999	9 Jul. 2001	170
	404	6867	29 Dec. 1998	16 Jul. 2002	250
Arequipa post-seismic	404	6867	31 Jul. 2001	16 Jul. 2002	150

Table 5.1: ERS and JERS interferograms used to constrain co-seismic and post-seismic deformation from the 2001 M_w 8.4 Arequipa, Peru, earthquake and the 1996 M_w 7.7 Nazca, Peru, earthquake.

We have made interferograms from four ERS orbital tracks (two descending and two ascending) for the 2001 earthquake (Figure 5.4). We measure a maximum deformation in the LOS of about 0.70 m. These interferograms also include inter-seismic (up to 5.5 years) and post-seismic deformation (Table 5.1). In addition, all of the co-seismic interferograms include the M_w 7.6 aftershock on July 7, 2001 (Figure 5.5). There are gaps in our coverage of the large deformation field of this earthquake
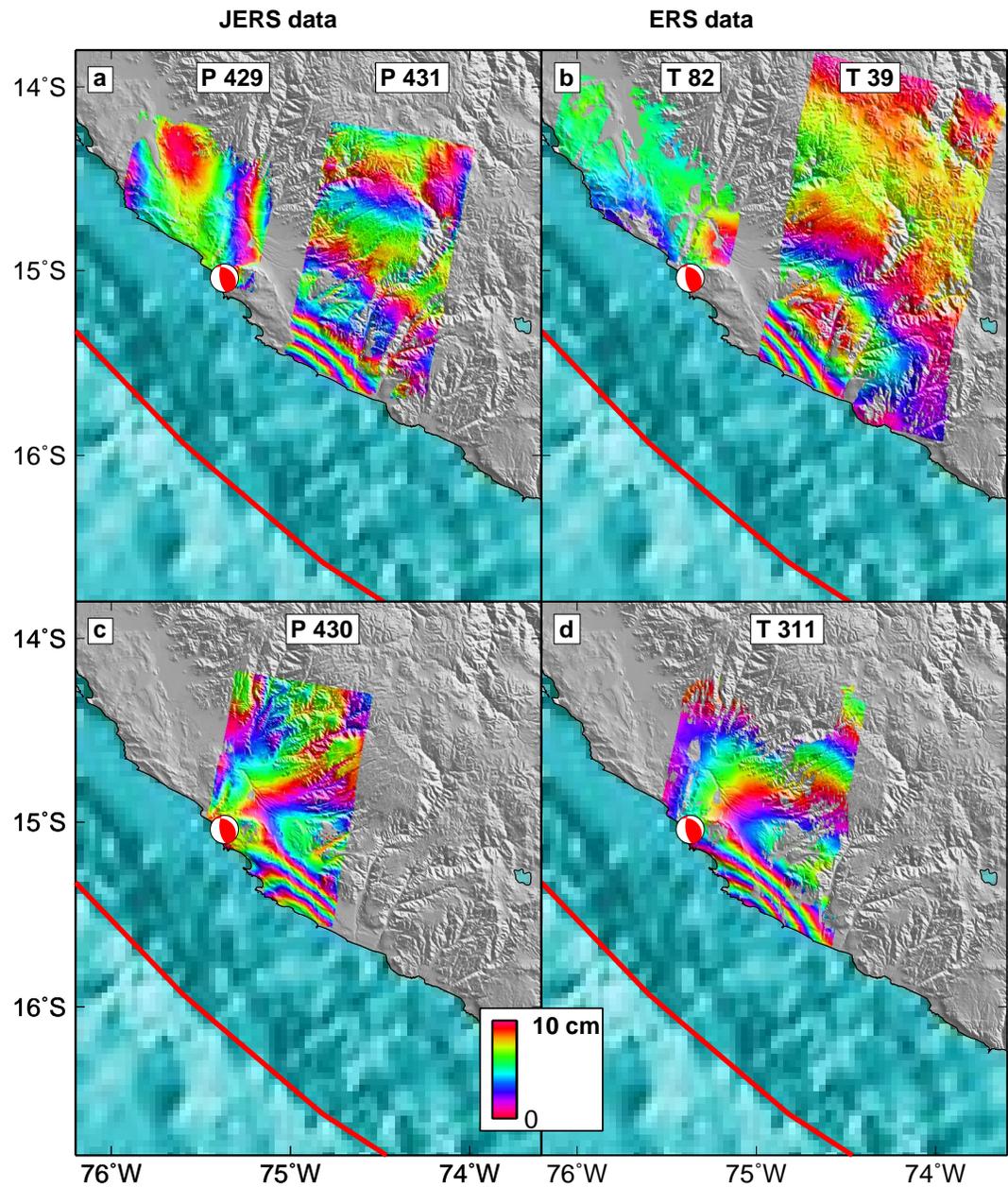
Figure 5.3: a. JERS interferograms of the 1996 M_w 7.7 Nazca, Peru, earthquake from paths 431 and 429 are shown. See Table 4.1 for dates of interferograms. b. ERS interferograms of the same earthquake from tracks 82 and 39 are shown. c. This is the JERS interferogram from path 430. d. Interferogram from ERS track 311. An M_w 6.1 aftershock on 2/9/1997 at 20 km might cause some of the deformation in track 82 and path 431.

because we were unable to make interferograms for some orbital tracks because of instrument problems with the data collected by ERS-2 in 2001 and 2002.

The data from a continuous GPS station in Arequipa, Peru, (about 200 km from the CMT location, see Figure 5.4 and Figure 5.5) is publically available, and provides constraints on the vector co-seismic (-0.42 m, -0.29 m, and -0.04 m, for the east, north and vertical components, *Ruegg et al.*, 2001; *Melbourne and Webb*, 2002) and post-seismic deformation. Additionally, there are at least 14 campaign GPS measurements of co-seismic displacement (*Norabuena et al.*, 2001), and another continuous GPS station (*Melbourne and Webb*, 2002) within the rupture area of this earthquake.

5.4 Modeling strategy

We use the InSAR and GPS data to invert for fault slip for the 1996 and 2001 earthquakes. For both earthquakes, we prescribe the fault geometry and perform the calculations in an elastic half-space. The location of the fault interface between the South American and Nazca plates is not as well defined in southern Peru as in northern Chile (Chapter 3). The slab dip is about 30° (*Hasegawa and Sacks*, 1981), but the detailed shape of the interface, particularly the variations of dip as a function of depth are not well known (*Spence et al.*, 1999). Based on relocated aftershocks from the 1996 earthquake a hinge in the plate at 25 km is suggested, where the slab dip changes from 10-12° to 25-55° (*Spence et al.*, 1999). The dip of our fault plane changes from 15° near the trench to 40° beneath dry land. We constrain the updip location of the fault to be at the trench (Chapter 3). Because the 1996 earthquake occurred near the location where the Nazca Ridge is subducting, there is some complexity in defining the trench location. The ridge is 1.5 km above the surrounding ocean floor (*Schweller et al.*, 1981), so there will be undulations of the fault interface, but the magnitude and location of these undulations are not constrained. Based upon bathymetric data (*Schweller et al.*, 1981), we assume that the trench in the area of the 1996 earthquake is 6 km deep, and 7 km in the location of the 2001 earthquake.

We constrain our inversions to have a rake similar to the plate convergence di-
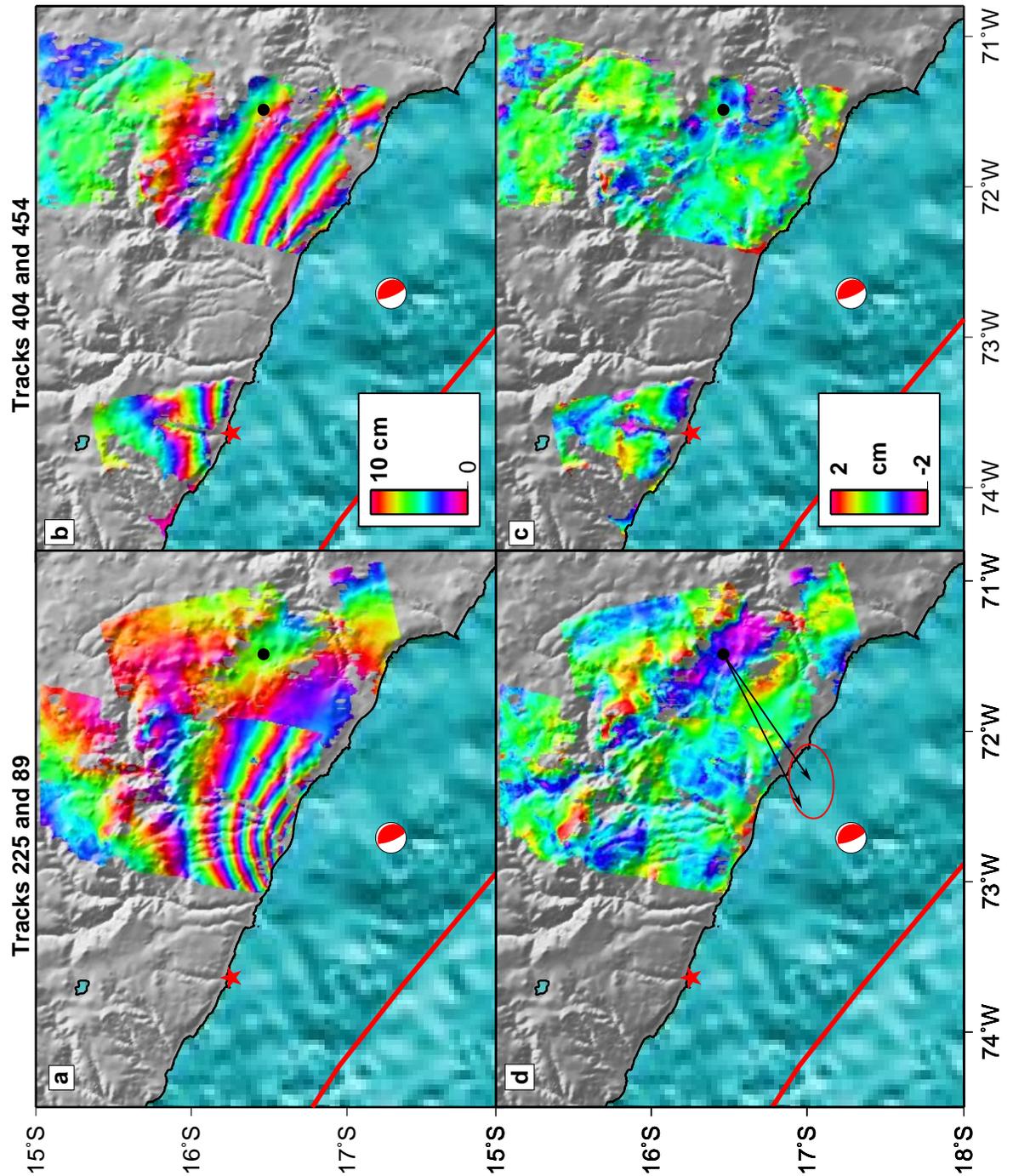
Figure 5.4: a. and b. Interferograms from four orbital tracks spanning the 2001 earthquake (see Table 5.1 for dates). The trench (red line), CMT location (red mechanism), hypocenter (NEIC – red star), and location of the Arequipa GPS station (black circle) are also shown. c. and d. Residuals from our best fit model (Figure 5.6), shown at a different color scale than in a and b. The co-seismic displacement at the Arequipa GPS station (*Melbourne and Webb*, 2002), the error ellipse, and model prediction are shown in c. RMS values: track 404, 1.1 cm; track 89, 1.0 cm; track 454, 0.8 cm; track 225, 0.7 cm.
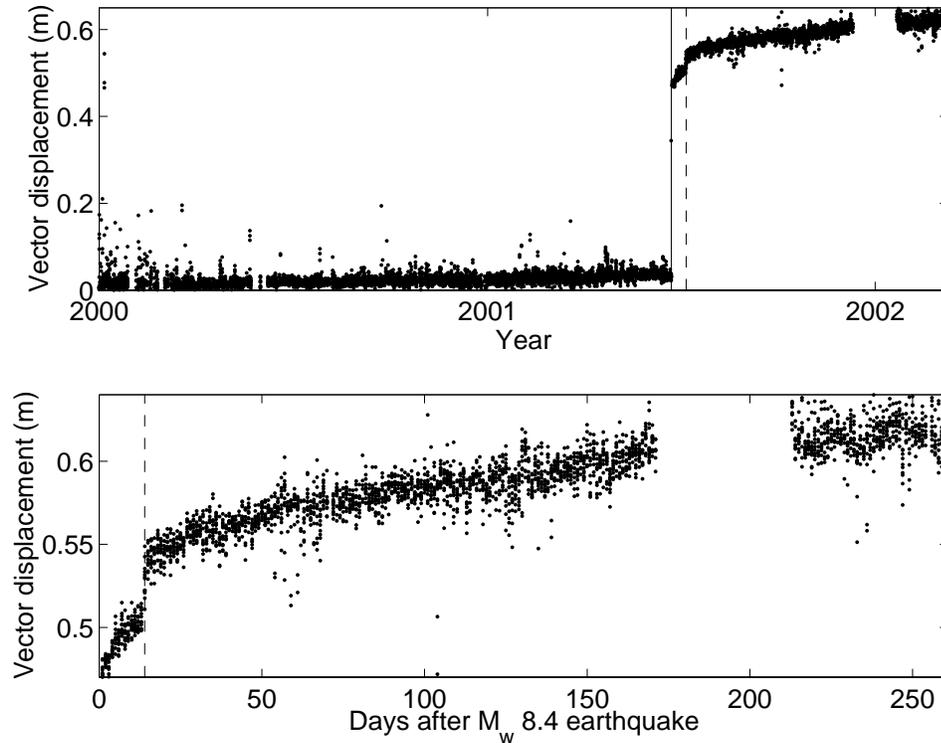
Figure 5.5: Vector GPS displacements at the continuous Arequipa station calculated every two hours. Top: Displacements 1.5 years prior to and nine months after the June 23, 2001 M_w 8.4 earthquake (shown as the solid line). The dashed line shows the large after shock M_w 7.6 on July 7, 2001. The co-seismic offset is 0.44 m from the M_w 8.4 earthquake and about 0.03 m from the M_w 7.6 event. Bottom: Zoom into the displacement time series shown above, showing the about 0.12 m of post-seismic deformation. Data processed by Tim Melbourne (*Melbourne and Webb*, 2002).

rection (77-80°) and previous inversions for these events using programs from the MATLAB Optimization Toolbox. We empirically select a Laplacian smoothing parameter by making a plot of model misfit as a function of roughness, and selecting a value that minimizes both values. While these so-called trade-off curves are commonly used, they can over-smooth the solution, but do not change the broad scale properties of the earthquakes that are of interest here (e.g., *Árnadóttir and Segall*, 1994). We discretize the fault plane with uniform patches (16 along strike and 10 in dip) that are 23 by 20 km for the 2001 earthquake and 19 by 20 km for the 1996 event. When calculating the InSAR displacements, we account for the variations in the incidence angle across the radar scene, which changes from 19°-28° for ERS and 35°-42° for JERS. In addition to estimating the strike-slip and dip-slip displacement for each subfault, we estimate a quadratic ramp for each interferogram to account for orbital errors and inter-seismic deformation (Chapter 3).

5.5   Results

5.5.1   1996 earthquake

We show our ERS and JERS InSAR slip distribution for the 1996 earthquake in Figure 5.6, and the residual interferograms in Figure 5.7. In this particular inversion, we have equally weighted the two types of InSAR data, but we experimented with different weighting, because the relative sensitivity of ERS and JERS is not known. Because of a problem shortly after launch, JERS transmits about one-quarter as much power as it was designed to, but this seems to have only a small effect upon the signal-to-noise ratio (e.g., *Murakami et al.*, 1996). For example, estimates of the intrinsic noise in the JERS radar system upon deformation measurements range from 0.3-1 cm (*Murakami et al.*, 1996; *Tobita et al.*, 1998). In several locations, JERS measurements of deformation agree with ground-based measurements – leveling: RMS of 1.5 cm on the Izu Peninsula, Japan (*Fujiwara et al.*, 1998); GPS: RMS of 1 cm in horizontal, 5 cm in vertical for the Mt. Iwate, Japan earthquake (both ascending and descending

InSAR used to estimate deformation components); RMS of 1.3 cm for Northridge, California earthquake (*Murakami et al.*, 1996). A difference of 10's of cm between JERS measurements and leveling was seen at Iwo Jima volcano (*Ohkura*, 1998), but a detailed error analysis was not done. The accuracy of JERS orbital locations is much poorer than for ERS, and in order to create images for use in modeling, we had to remove a co-seismic model (derived from the ERS data) from each interferogram and re-estimate the baseline parameters that minimize the residual phase variations (Chapter 3).

From the inversion with equal weighting, the RMS residuals from JERS and ERS are about the same (1 cm, see Figure 5.7), and indicate that previous estimates of the JERS error budget are too conservative for our observations (4.2 cm, *Murakami et al.*, 1996). Our small residual between the JERS data and the model is much less than in previous studies (10's of cm) of the earthquakes of Northridge, California, Sakhalin Island, Kobe, Japan, and Mt. Iwate, Japan (*Murakami et al.*, 1996; *Massonnet et al.*, 1996; *Tobita et al.*, 1998; *Ozawa et al.*, 1997; *Fujiwara et al.*, 2000).

We constrain the rake to be between 0-90°, and found the average rake to be 82° for all patches, but only 63° for the patches with slip > 1 m. The CMT rake is 52°, or 50° $\pm$ 15° from the only previous inversion that calculated the rake instead of assuming this value (*Salichon et al.*, 2003). The maximum slip is about 1.5 m, but both the maximum slip and the seismic moment are model dependent and sensitive to the choice of smoothing value. Previous inversions have found a wide range of seismic moments. Moments from seismic-only inversions are: 2.4-3.5 $\times$ 10^{20} Nm (M_w 7.5-7.6) (*Swenson and Beck*, 1999); 1.5 $\times$ 10^{21} Nm (M_w 8.0) (*Spence et al.*, 1999). *Salichon et al.* (2003) performed InSAR only (one track of data), seismic only, and joint inversions, and found a moment of 4.1 $\times$ 10^{20} Nm (M_w 7.7) for the InSAR or seismic inversions and 4.4 $\times$ 10^{20} Nm (M_w 7.7) for the joint inversion. When we place equal weight on the ERS and JERS data, the seismic moment is 7.4 $\times$ 10^{20} Nm (M_w 7.9), or 6.7 $\times$ 10^{20} Nm (M_w 7.8) if the tensor sum is calculated (see Chapter 3). If we weight the ERS data twice as much as the JERS data, the moment is 6.5 $\times$ 10^{20} Nm (M_w 7.8) or the tensor moment is 5.6 $\times$ 10^{20} Nm (M_w 7.8).
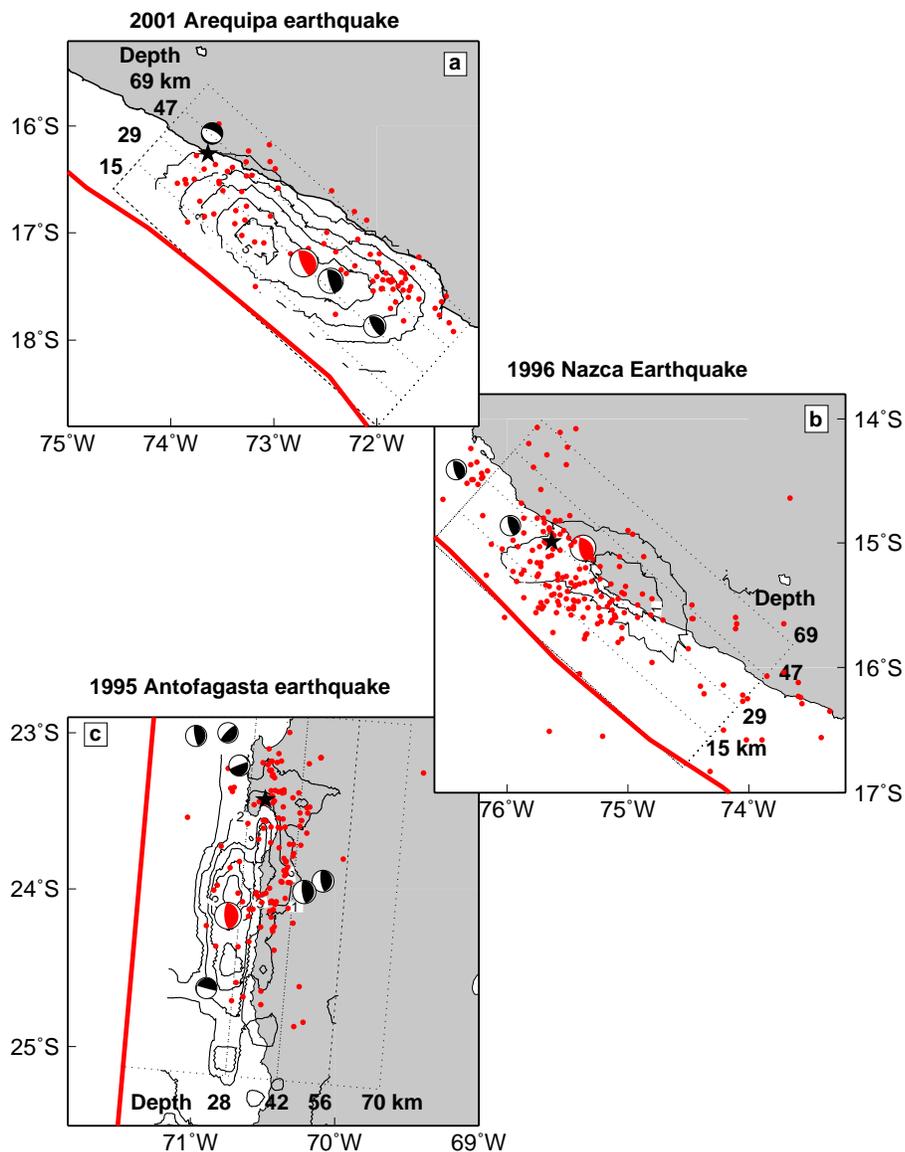
Figure 5.6: Contours of slip from the 1996 and 2001 Peru, and 1995 Chile earthquakes. In all maps, the black stars are the NEIC locations for the main shocks, red mechanisms are for the main shocks, red circles are aftershock locations, black lines show depth intervals on the slab, red lines are the trench, and black mechanisms are CMT's with $M_w > 6$. a. The 2001 earthquake is shown with slip contours every 1 m with relocated small aftershocks from *Giovanni et al.* (2002). b. The 1996 earthquake with contours every 0.5 m. Aftershocks are from the NEIC catalog between 11/12/1996-6/23/01. c. The 1995 earthquake with contours every 1 m (from the joint seismic and geodetic inversion Figure 4.7). Aftershocks with $M_w > 2.5$ were located by a local network (*Husen et al.*, 1999). Harvard CMT mechanisms for the 1996 and 1998 earthquakes have been shifted to the east to the NEIC location (see Chapter 4).
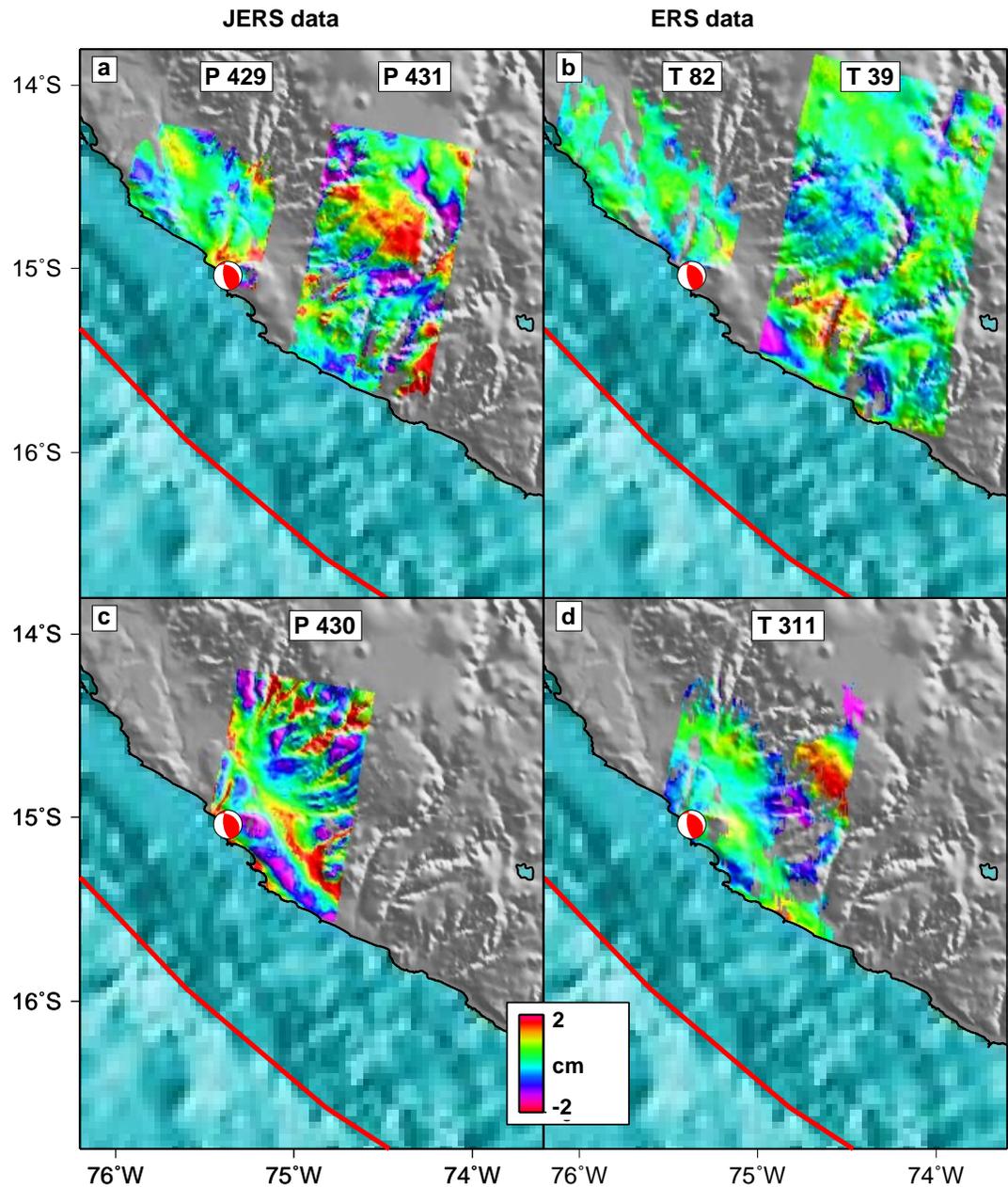
Figure 5.7: InSAR residuals from our best fit model for the 1996 earthquake (data from Figure 5.3, model from Figure 5.6 – equal weighting of ERS and JERS). a. JERS paths 429 and 431. b. ERS tracks 82 and 39. c. JERS path 430. d. ERS track 311. RMS values – track 311: 0.9 cm; track 39: 0.7 cm; track 82: 0.4 cm; path 429 0.013 m; path 430 1.3 cm; path 431: 0.8 cm. For the sake of comparison, the shaded relief in Figure 5.3 is from SRTM (90 m/pixel), while in this figure the resolution is 900 m/pixel – from the highest resolution DEM of the area available before SRTM.

Part of the variation in seismic moment between the seismic and geodetic results could be due to the different rigidities used.

5.5.2   2001 earthquake

We show the slip from the 2001 earthquake in Figure 5.6 and the GPS prediction with InSAR residuals in Figure 5.4. We equally weight the InSAR observations, but give a greater weight to the Arequipa GPS station (factor of 1.5-3.3 depending on the error for each component). Because of a large orbital ramp for track 89, we performed an initial inversion for the other scenes, and completed the procedure of re-estimating the baselines as mentioned above for the JERS data. In any case, the deformation signal in this track is small (Figure 5.4). Because only a portion of the deformation field is measured by each satellite track, there is a trade-off between the slip and the ramp parameters. In the future, we hope to reduce this trade-off by using the azimuth offsets to measure the horizontal deformation. Our model predicts that the peak-to-peak amplitude of the azimuth offsets would be between 30-60 cm (depending on the orbital track), which should be detectable given that the error on the measurements is between 10-40 cm (e.g., *Michel et al.*, 1999a,b; *Jónsson*, 2002; *Simons et al.*, 2002).

The maximum slip in our model is 6 m and both the moment and tensor moment are 4.1×10^{21} Nm (M_w 8.3). Previous moment estimates based on seismic data are: 4.7×10^{21} Nm (M_w 8.4) Harvard CMT; 2.4×10^{21} Nm (M_w 8.2) (*Giovanni et al.*, 2002); 6.3×10^{21} Nm (M_w 8.5) (*Bilek and Ruff*, 2002). The 2001 event is the largest global earthquake since at least the 1977 Sumbawa, Indonesia, event, (2.4-7.9 $\times 10^{21}$ Nm – M_w 8.2-8.5, *Lynnes and Lay*, 1988; *Zhang and Lay*, 1989), and perhaps since the 1965 Rat Island, Alaska, event (14×10^{21} Nm – M_w 8.7, *Wu and Kanamori*, 1973). We constrain the rake between 50° and 80° and find a mean value of 71° with a weighted average of 74°. The CMT rake is 63° and *Bilek and Ruff* (2002) found a rake of 75°. *Ruegg et al.* (2001) used the Arequipa GPS station to find a moment of 4.4×10^{21} Nm (M_w 8.4) and a rake of 123°.

5.5.3 Post-seismic deformation 1997-1999

We have three interferograms that span the time period between the 1996 and 2001 earthquake (Figure 5.8). We have made interferograms spanning 1/2/1997-12/23/1999 from two orbital tracks, but no measurements of deformation exist during the first 51 days following the earthquake. The interferograms do not show any obvious post-seismic deformation, although long-wavelength deformation would be removed by the process of baseline re-estimation. The phase variations in the interferograms appear to be either random or correlated with topography, indicating atmospheric contamination (Chapter 4).

5.5.4 Post-seismic deformation 2001-2002

About 12 cm of post-seismic vector displacement is recorded at the Arequipa GPS station during the first nine months following the 2001 earthquake (Figure 5.5, *Melbourne et al.*, 2002; *Melbourne and Webb*, 2002). Because of the rapid timescale involved, this deformation is inferred to be the result of down-dip afterslip (Chapter 4). The moment release during this post-seismic time interval ($\sim$ 20% of the co-seismic moment) is much more than the moment released following the 1996 and 1995 earthquakes (Table 4.2).

We have made only one interferogram from track 404 that spans the post-seismic time interval (Figure 5.9), and it does not show any clear deformation. However, there was a large orbital ramp in these scene which we removed by baseline re-estimation, and if the post-seismic deformation had a similar wavelength to the orbital errors, we might have removed a real deformation signal (Chapter 4). It is also possible that this track is not optimally located to capture the post-seismic deformation. Track 404 is located near the hypocenter, where there was little co-seismic moment release in our smooth geodetic inversion. Seismic inversions indicate one of the two large asperities from the earthquake is at this location near the hypocenter (*Giovanni et al.*, 2002; *Bilek and Ruff*, 2002).

There is little hope of extracting additional post-seismic deformation from the ex-
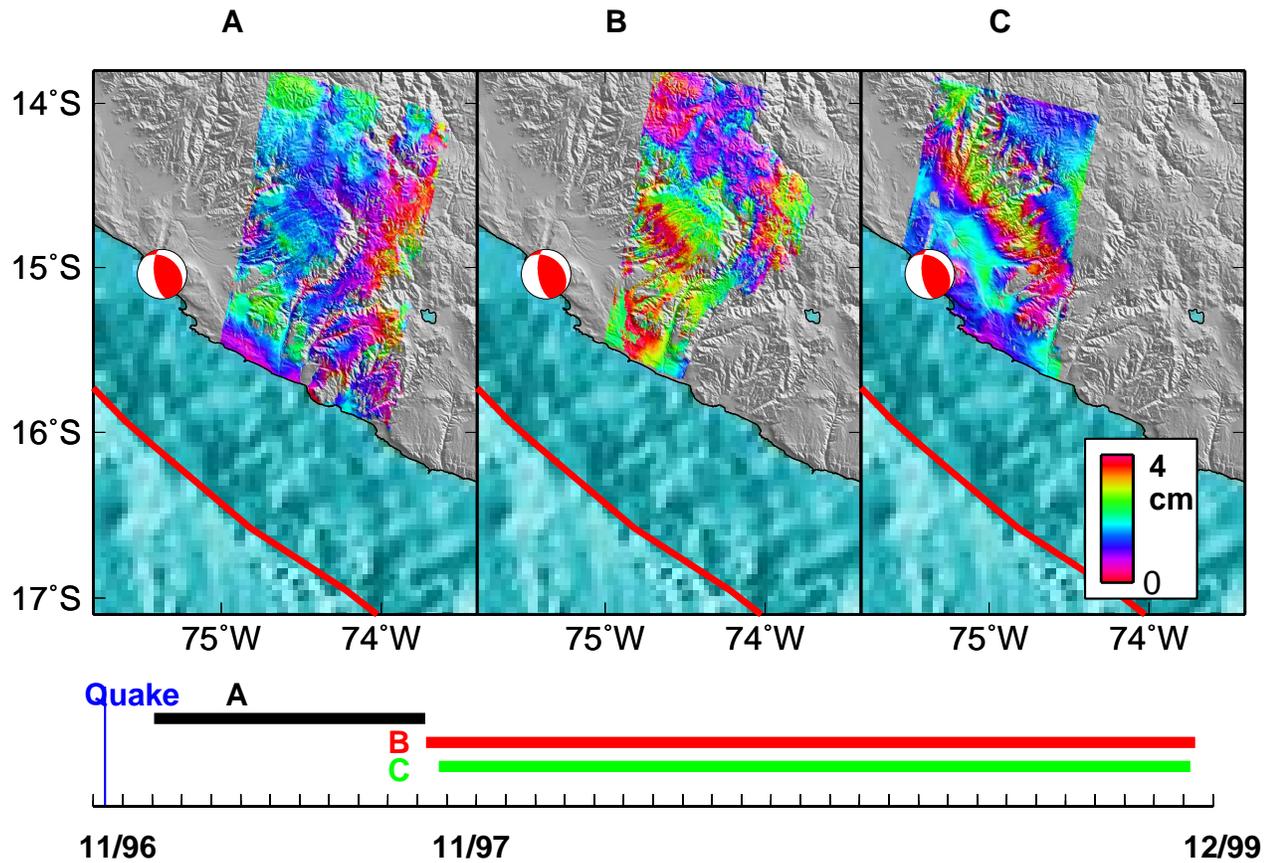
Figure 5.8: A. and B. Post-seismic ERS interferograms following the 1996 earthquake from track 39. C. Interferogram from ERS track 311 spanning the post-seismic time interval after the 1996 earthquake. Below the interferograms, we show the time periods of the interferograms (Table 5.1) compared to the time of the earthquake. These interferograms show no obvious deformation.

Track 404: 7/31/01-7/16/02
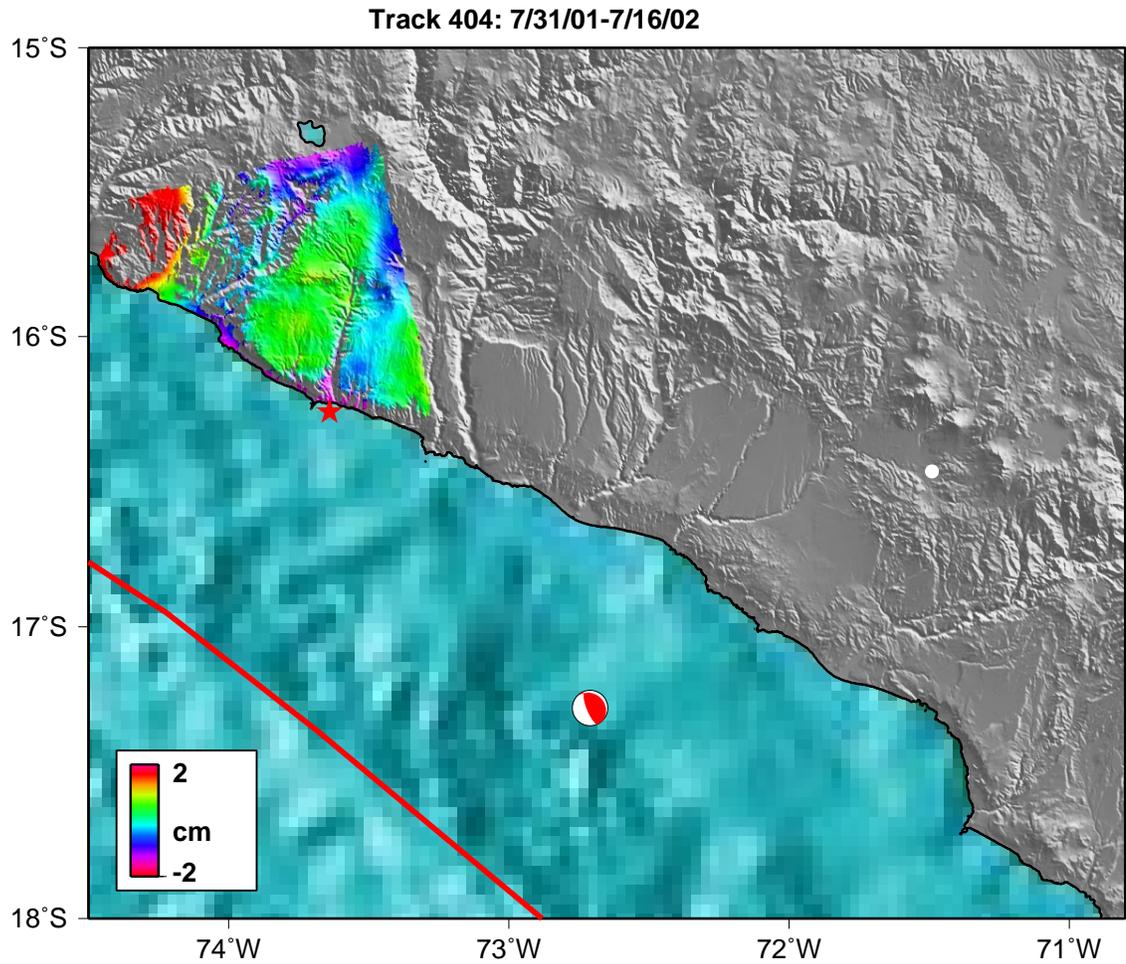
Figure 5.9: Interferogram from track 404 spanning 7/31/01-7/16/02, that shows no obvious post-seismic deformation. However, part of the deformation signal might have been lost by removing orbital ramps (see text). White circle shows the location of the Arequipa GPS station that has large post-seismic displacements (Figure 5.5).

isting InSAR dataset (Table 5.1). In principle, each interferogram contains a different amount of post-seismic deformation, and so an inversion of each individual track could allow for independent estimates of the fault slip in a given location. Comparision of the slip maps could reveal how much slip was co-seismic and post-seismic. However, because of the non-uniqueness of the problem, particularly because of the trade-off between slip and orbital parameters for this event, this type of track to track comparison will not unambiguously reveal the post-seismic slip.

5.6   Discussion

We compare the slip distributions for the 1995, 1996, and 2001 earthquakes in Figure 5.6. Our smoothed geodetic only inversions reveal the gross properties of the slip in the 1996 and 2001 earthquakes, and do not reveal the localized regions of slip seen in the seismic inversions (*Swenson and Beck*, 1999; *Salichon et al.*, 2003; *Spence et al.*, 1999; *Giovanni et al.*, 2002; *Bilek and Ruff*, 2002). Nonetheless, our slip model is similar to previous results in seismic moment, rake and general slip distribution, and probably better resolves the bottom limit of the rupture.

We define the bottom of the co-seismic rupture as the location of the 0.5 m contour on our slip maps. For the 1996 earthquake, our maximum depth is 60 km, which lies between previous estimates of 40 km (*Salichon et al.*, 2003) and 66 km (*Spence et al.*, 1999). We find a maximum depth of 45 for the 1995 event, which is similar to the 40 km of *Ihmlé and Ruegg* (1997) and 50 km of (*Klotz et al.*, 1999). The 2001 earthquake ruptured to a maximum depth of between 50-60 km. We favor the smaller value because the slip goes deeper in the northeast part of rupture where there is less data, and there are also possible effects from the M_w 7.5 aftershock. The bottom of the 2001 and 1995 earthquakes is close to the location of the coastline, and as noted in Chapter 4, the coastline might control the down-dip limit of the seismogenic zone. The 1996 earthquake ruptures further beneath land than the other two events, and this might be related to subduction of the Nazca ridge. The CMT depth of the 1996 event is also the deepest – 37.4 km compared to 28.7 km and 29.6 km for the 1995

and 2001 earthquakes, respectively.

5.6.1 Aftershocks

Comparing the location of slip in a large earthquake with the distribution of after-shocks provides clues to the stress level on the fault interface. For example, if after-shocks occur in the same location as large amounts of slip, it might indicate asperities on the fault interface (e.g., *Lay and Wallace*, 1995). In contrast, an anti-correlation between the location of slip and aftershocks has been interpreted to suggest that the regions around the earthquake were stressed to the point of failure by the earthquake or post-seismic deformation (e.g., *Deng et al.*, 1999). It is difficult to compare the location of rupture to the distribution of aftershocks for the three events, because only the 1995 aftershocks have been well located by a local on-shore and off-shore network. Teleseismic data was used to relocate the 2001 aftershocks (Figure 5.6, *Giovanni et al.*, 2002) and a local network was used to locate the 1996 aftershocks *Spence et al.* (Figure 6 of 1999). The relationship between slip and aftershocks for the 1995 earthquake is more obvious in Figure 5.6 than Figure 3.10. Most of the aftershocks appear at the north-east down-dip edge of the co-seismic rupture. For the other earthquakes, the relationship is less obvious, although the aftershocks from the 1996 earthquake are mostly confined to the Nazca ridge, and the 2001 aftershocks might be located at the edges of the co-seismic rupture. A local network was occupied following the 2001 earthquake, so better relocations will be possible (*Tavera et al.*, 2001).

The distribution of large aftershocks ($M_w > 6$) is different for the three events. For 1995, the largest aftershocks occur down dip of the co-seismic rupture up to 2.5 years after the event. In fact, in northern Chile, several large earthquakes seem to rupture the area down-dip of the 1995 event (Chapter 4), indicating that this earthquake did not rupture the entire seismogenic zone. Following the 1996 and 2001 earthquakes, the largest aftershocks were either at the same depth or shallower than the region that ruptured in the mainshock. One large aftershock from the 2001 event did occur

down-dip from the region of large slip, but has a normal mechanism and might not have occurred on the fault interface. The aftershock distribution for the 1996 and 2001 events is consistent with these earthquakes rupturing the entire seismogenic zone. The depth of the seismogenic zone in southern Peru is poorly constrained, but the deepest events (only a few are known) occur at about 60 km (*Stauder*, 1975), and an examination of focal mechanisms indicates a change in the stress regime around 60 km (*Tavera and Buforn*, 2001).

5.6.2   Directivity

The 1995, 1996, and 2001 earthquakes all rupture unilaterally to the south (e.g., *Ruegg et al.*, 1996; *Swenson and Beck*, 1999; *Giovanni et al.*, 2002, Chapter 4). In fact, several earthquakes south of about 12°S rupture unilaterally to the south: the 1974 M_w 8.1 Peru event (bilateral, but most moment to south, *Langer and Spence*, 1995); the 1985 M_w 8.0 Chile event (ruptured updip and to the south, *Choy and Dewey*, 1988; *Mendoza et al.*, 1994); and the 1960 M_w 9.5 Chile event (ruptured "away from Pasadena," in Benioff's words, *Benioff et al.*, 1961). Earthquakes in other parts of the South American subduction zone do not rupture to the south – earthquakes in northern Peru are bilateral, such as the 1996 M_w 7.5 Peru earthquake (e.g., *Ihmlé et al.*, 1998) and the 1966 M_w 8.0 Peru event (*Beck and Ruff*, 1989), while earthquakes in Colombia and Ecuador rupture to the north, such as 1979 M_w 8.2 Colombia event (*Kanamori and Given*, 1981; *Beck and Ruff*, 1984). It has not been possible to determine the directivity of events before 1960 (*Swenson and Beck*, 1996).

Thus, it seems that there is a pattern of earthquake directivity in South America – in the north, earthquakes rupture to the north, in the middle, earthquakes are bilateral, and in the south, directivity is southerly. We can only speculate on the mechanism for this variation, because the factors that control earthquake directivity are poorly understood. In a global study, *McGuire et al.* (2002) find that most earthquakes are unilateral, and think that fault segmentation might explain this observation for large earthquakes. If earthquake ruptures can nucleate anywhere along

strike and are terminated by fault irregularities, then most ruptures will be unilateral (*McGuire et al.*, 2002). However, no explanation is given for ruptures favoring one direction over the other (*i.e.,* the preference for ruptures to the south in southern South America). One possibility is that history is important. Perhaps the process of oblique convergence or previous earthquake ruptures developed a fabric on the fault interface that favors rupture in one direction. The direction of convergence relative to the trench varies systematically from northern to southern South America, so this type of mechanism could explain the observation. Another possibility is that the material contrast between the two sides of the fault controls the direction of rupture (e.g., *Rubin and Gillard*, 2000). A variety of experiments show that a rupture will prefer to go in the direction that the weaker material is slipping (for references, see *Rubin and Gillard*, 2000). *McGuire et al.* (2002) argue that because subduction zone earthquakes are primarily thrust events, this effect would favor along-dip, but not along-strike directivity. Further work is need to see if oblique convergence (as occurs in South America) can cause a second order effect that favors along-strike directivity.

5.6.3 Afterslip

The amount of afterslip following the 1996 and 1995 earthquakes is anomalously low compared to other recent subduction zone earthquakes and the 2001 event (Table 4.2). To understand the possible cause of the different amounts of afterslip, we first review the canonical model for the mechanics of the process (for a review, see *Scholz*, 1990; *Marone et al.*, 1991; *Scholz*, 1998). Faults are made up of materials with different frictional properties. Some parts of the fault are unstable to frictional sliding, and so move in a stick-slip fashion during an earthquake (*i.e.,* velocity-weakening). Other parts of the fault are stable to sliding (*i.e.,* velocity-strengthening) – they will not move during an earthquake, but if they are loaded by the earthquake they will slowly relax.

Afterslip is thought to occur in regions that are velocity-strengthening. Temperature and pressure are two important parameters that control the frictional behavior,

and so afterslip might occur down-dip of the co-seismic rupture where the fault interface becomes too pressurized or hot to slip during the earthquake. For some events, afterslip appears to be down-dip of the earthquake (*Hutton et al.*, 2002; *Yagi et al.*, 2001) or begin in nearly the same location as the co-seismic slip (*Heki et al.*, 1997, but the resolution of slip at this location is crude) and migrate deeper with time (*Nishimura et al.*, 2000). In other locations, the afterslip seems to be at the same depth as the co-seismic slip, but shifted along strike (Chapter 4). It is also possible that co-seismic slip or afterslip can trigger silent slip on an another part of the fault interface (*Miyazaki et al.*, 2003). Of course, some afterslip can not be localized because of poor station coverage (e.g., *Bürgmann et al.*, 2001, 2001 Peru earthquake). Other factors can control the frictional properties – variations in the topography on the ocean floor (e.g., seamounts), or in composition of sediments or the overriding plate (e.g., *Pacheco et al.*, 1993).

Before continuous GPS observations demonstrated the ubiquity of afterslip (Table 4.2) and silent slip events (e.g. *Lowry et al.*, 2001b; *Dragert et al.*, 2001; *Miller et al.*, 2002; *Ozawa et al.*, 2002), many workers postulated that there is significant aseismic deformation at subduction zones (e.g. *Kanamori*, 1977; *Peterson and Seno*, 1984; *Pacheco et al.*, 1993). These authors note a discrepancy, in some subduction zones, between the slip predicted by global plate tectonic models and the slip observed in earthquakes. The ratio of the seismic moment release to the predicted moment release based on plate motion is called the seismic coupling coefficient (α). Values of α range between zero (slip on the fault interface is completely aseismic) to one (the subduction zone is fully coupled). The slip deficit in partially coupled zones could be accommodated as afterslip, deformation immediately before an earthquake, or silent slip events independent of an earthquake. However, because the time span of observations is much shorter than the earthquake recurrence time for most regions, it is difficult to compare the values of α between subduction zones. In fact, the global compilation of α can be fit with a constant value of 0.3, with the variations between subduction zones explained by different recurrence times (*McCaffrey*, 1997). The large uncertainty in α makes any possible correlation between the coupling coefficient

and the magnitude of afterslip difficult to see (Table 4.2). Furthermore, α is basically identical for southern Peru and northern Chile, so no variation in the magnitude of afterslip within our study area was anticipated.

In order to understand the along-strike variations in afterslip in our study area, it is useful to think of two end-member scenarios: either the earthquakes are different, but the fault properties are the same; or the earthquakes are similar, and the fault properties are different. The earthquakes and fault properties are undoubtedly not identical for all three areas, but which difference is the most important? If the frictional properties are only controlled by depth, there might be variations in afterslip if each earthquake loaded the frictionally stable region in a different way. For example, an earthquake that ruptured into the stable region would have more afterslip than an earthquake that did not. One hypothesis is that the the bottom of the seismogenic zone corresponds to a transition from unstable to stable sliding (e.g., *Pacheco et al.*, 1993). In general, the specific earthquakes that have afterslip (see Table 4.2 for references) seem to rupture to the bottom of the seismogenic zone (as defined by prior seismicity, *Zhang and Schwartz*, 1992; *Tichelaar and Ruff*, 1993b; *Oleskevich et al.*, 1999), but the depth of the seismogenic zone and the depth of earthquakes are poorly constrained in several locations. Furthermore, the depth of the seismogenic zone might be time dependent or depend on the size of the earthquake. For example, some regions of the fault might be "conditionally stable" (e.g., *Pacheco et al.*, 1993), where earthquakes cannot nucleate, but that can slip co-seismically when triggered by a large earthquake.

If we assume that the stable region begins where the seismogenic zone ends, the variation in the depth of rupture will not explain the afterslip variations that we observe. As mentioned above, it seems that while the 1995 earthquake did not rupture to the bottom of the seismogenic zone, both the 1996 and 2001 earthquakes did. However, the 2001 event had afterslip, and the 1996 event did not. The Nazca Ridge could complicate the 1996 rupture area, but this leads us to the second end-member – that variations in the earthquake are not as important as variations in the fault properties.

In addition to the presence of the Nazca Ridge near the 1996 earthquake and a smoother fault interface for the 1995 and 2001 earthquakes, there is an along-strike variation in the amount of sediment subducted. There is virtually no sediment off Antofagasta due to the arid on-shore climate, no sediment on the Nazca ridge, but there are sediments in the Arequipa rupture zone (Figure 4 in *Schweller et al.*, 1981). The sediment in the Arequipa rupture area might have enhanced afterslip in that location. Other properties of the subduction interface are similar in the three rupture areas – in southern Peru the Nazca plate is about 38-43 million years old (*Müller et al.*, 1997) and the rate of convergence is 5.9 cm/yr at 14°S and 77°W (*Angermann et al.*, 1999); while in northern Chile the Nazca plate is about 45 million years old and the convergence rate is 6.3 cm/yr at 24°S, 71.4°W.

If the amount of sediments really do control the rupture properties, we would expect there to be very little afterslip following the earthquake that re-ruptures the location of the 1877 earthquake, because of the lack of sediment in that area. The event that ruptures the 1877 gap will lie between the 2001 and 1995 earthquakes, and so it will also be interesting to see if this event ruptures to the bottom of the seismogenic zone in the main shock (like the 2001 event) or during the aftershock sequence (like the 1995 event).